Energy Storage Materials 48 (2022) 458–465

Contents lists available at ScienceDirect

Energy Storage Materials

journal homepage: www.elsevier.com/locate/ensm

Bipolar stackings high voltage and high cell level energy density sulfide based all-solid-state batteries

Daxian Cao, Xiao Sun, Ying Wang, Hongli Zhu*

Department of Mechanical and Industrial Engineering, Northeastern University, Boston, MA 02115, USA

ARTICLE INFO

Keywords:
Bipolar stacking
All solid-state batteries
Si anode
Amphipathic binder
Sulfide solid electrolyte
$LiNi_{0.8}Mn_{0.1}Co_{0.1}O_2$

ABSTRACT

Compared to the lithium-ion batteries using organic liquid electrolytes, all-solid-state lithium batteries (ASLBs) have the advantages of improved safety and higher energy density. Multilayered bipolar stacking in ASLBs can further improve the energy density by minimizing the use of inactive materials. However, it is highly challenging to fabricate bipolar stacked ASLBs because of lacking vigorous laminated electrodes and electrolyte, especially for sulfide solid electrolytes. This work successfully assembled bipolar stacked ASLBs with high voltage by facilely stacking freestanding and robust cathode, electrolyte, and anode sheets. More specifically, interface stabilized single-crystal $LiNi_{0.8}Mn_{0.1}Co_{0.1}O_2$, Li_6PS_5Cl, and nano Si act as cathode, electrolyte, and anode individually. Amphipathic ethyl cellulose plays a role as a disperser during ink preparation and further as a binder in the freestanding membranes. The doubly stacked ASLB delivers a high voltage of 8.2 V and cell-level energy density of 204 Wh kg^{-1} higher than the 189 Wh kg^{-1} of the mono cell.

1. Introduction

All-solid-state lithium batteries (ASLBs) using solid-state electrolytes (SEs) have prospectively higher energy density than conventional lithium-ion batteries (LIBs) using organic liquid electrolytes [1–3]. In addition to increasing the energy density in ASLBs by optimizing materials and structures in a single galvanic cell [4], a particular bipolar stacking design can deliver higher energy densities but lack attention. In industrial applications, like electric vehicles (EVs), batteries are packed either in series or parallel to maximize power and energy [5]. In a conventional LIBs system, each unit cell is sealed separately to avoid the leakage and internal ionic short circuit in the cell pack caused by the flowable liquid electrolyte. Therefore, many inactive materials, like the current collectors, packing materials, and wire tabs for external connections, are utilized in the battery system, significantly limiting energy density and increasing cost [6]. It is essential to reduce the usage of inactive materials to reduce the weight and cost [7]. In contrast, attributed to the solid feature, a unique bipolar design is feasible in ASLBs to minimize the usage of inactive materials and maximize the energy density [8,9].

Bipolar stacking is a configuration for battery pack where all the mono cells are connected in series through one current collector contacting two electrodes without external connections [8]. The nonflowing SEs can avoid the internal ionic short circuit. On one side, the usage of inactive material can be further reduced when the adjacent cathode and anode share one current collector. Meanwhile, the packing materials can be minimized because all the cells can be packed inside one package. Furthermore, the shortened electron conduction paths between mono batteries resulted in lower resistance and higher power density. In addition, the bipolar-stacked ASLBs can deliver a high output voltage enabling versatile applications. Currently, most reported bipolar-stacked ASLBs are based on solid polymer electrolytes or composite polymer electrolytes [10–14], in which the low ionic conductivity of SEs limits their performances for practical applications [14,15]. Meanwhile, the polymer-based electrolytes can melt and be flowable when the ASLBs run at a high temperature, resulting in an ionic short [16]. Given the high ionic conductivity (>1 mS cm^{-1}) and high thermal stability [2], sulfide SEs are one of the best candidates to fabricate bipolar-stacked ASLBs. However, sulfide SE-based bipolar-stacked ASLBs are rarely reported. The main challenge is fabricating compatible electrodes and SE layers with good film formability and mechanical strength to avoid the short circuit in cell fabrication.

In this work, we successfully fabricated high voltage ASLBs with a bipolar design based on sulfide SE. Benefiting from the amphipathic property, high binding capability, excellent compatibility with sulfide SE, and high thermal stability, the ethyl cellulose binder enables the successful fabrication of freestanding, robust, and thickness-controllable cathode, SE, and anode layers through vacuum filtration [17]. An interface stabilized high voltage single-crystal $LiNi_{0.8}Mn_{0.1}Co_{0.1}O_2$ (S-NMC) and nano Si were utilized separately as cathode and anode active material. The corresponding electrochemical performances of the ob-

* Corresponding author.
E-mail address: h.zhu@neu.edu (H. Zhu).

https://doi.org/10.1016/j.ensm.2022.03.012
Received 8 January 2022; Received in revised form 26 February 2022; Accepted 11 March 2022
Available online 15 March 2022

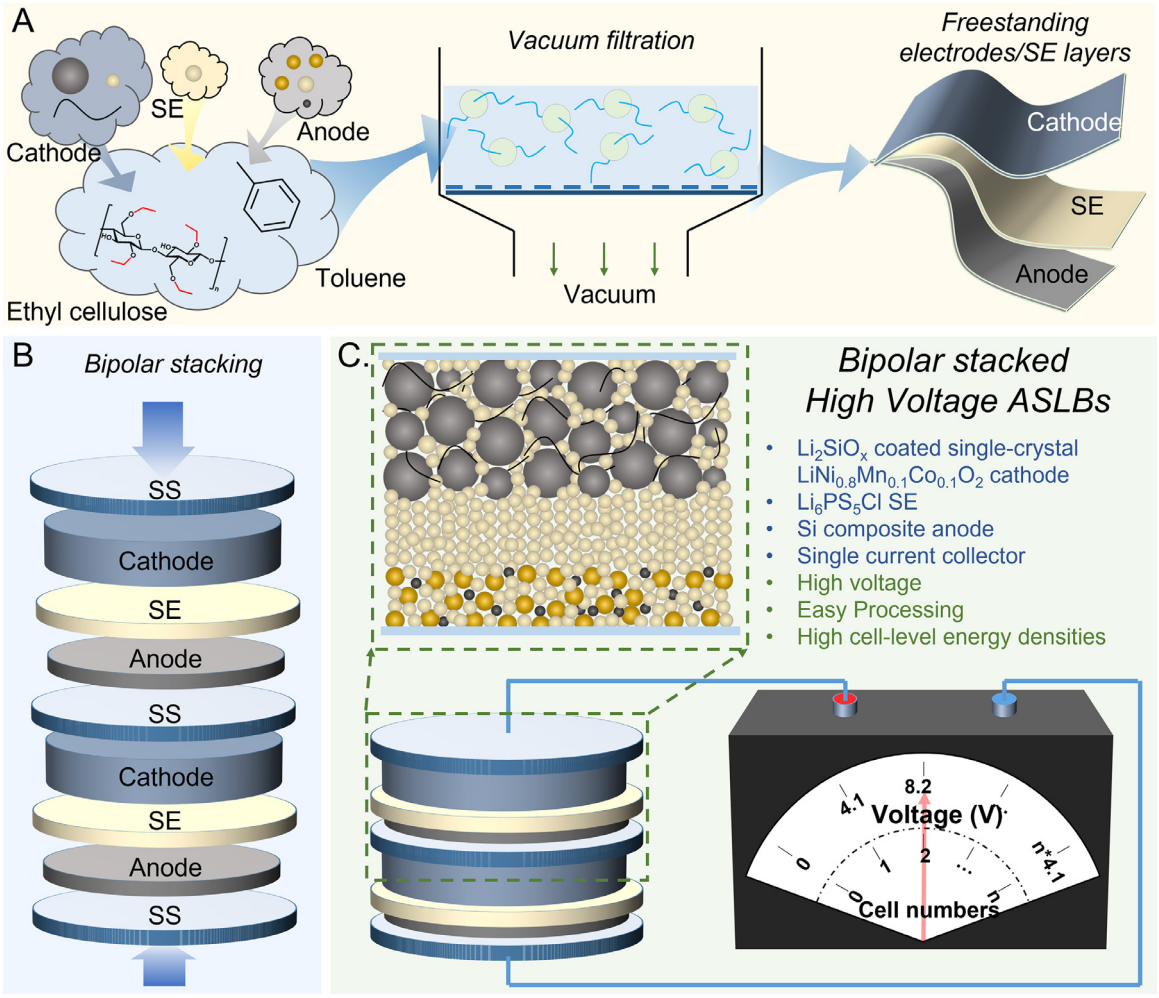

Scheme 1. Overview of this work. (A) The fabrication process of the freestanding cathode, SE, and anode layers via vacuum filtration. (B) The fabrication of bipolar stacked ASLBs through layer-by-layer stacking and followed with pressing. (C) Merits of the high voltage bipolar-stacked ASLBs and composition distribution in each layer.

tained electrode layers are investigated. Then the mono cell and bipolar-stacked double-layer cell were fabricated, and the electrochemical performances were evaluated. This work enlightens the research interest in investigating bipolar-stacked ASLBs and accelerates the development of ASLBs from laboratory scale to industrial manufacturing.

2. Results and discussions

Robust electrodes and SE layers play critical roles in bipolar stacked ASLBs fabrication. The electrodes and SE layers used for bipolar stacked ASLBs should own high integrity, well-controlled layer thickness/mass, high robustness to benefit the stacking of many cells. In most studies on sulfide SE, cold pressing is used to make thick pallets of electrode and SE. However, it faces the following limitations: First, it is difficult to obtain a thin and uniform membrane, resulting in an easy internal short circuit when stacking multiple cells; Second, the cold-pressed SE layer owns high thickness/mass causing a limited cell-level energy density. The cell size is also limited; Third, the consistency of each cell in bipolar stacked ASLBs highly determines the cycling stability and life. Meanwhile, it is challenging to accurately control each cell's consistency through cold pressing.

Scheme 1 illustrates the overview of our work. Aiming to fabricate the bipolar stacked ASLBs, we developed freestanding electrodes and SE layers through a vacuum filtration method. Our previous work successfully prepared an ultrathin SE membrane based on Li_6PS_5Cl with a low thickness of 47 μm and areal resistance of 4.32 Ω cm^{-2} [17]. With the same method, the electrodes layers were fabricated. As presented in Scheme 1**A**, the cathode, SE, anode powders were well dispersed in the toluene with the assistance of amphipathic binder ethyl cellulose. The ethyl cellulose enabled cathode and anode composites to be stably dispersed in toluene without precipitation, as shown in **Fig. S1**. Freestanding cathode, SE, and anode layers can be successfully prepared through vacuum filtration and are heated to remove the residual solvent. The layer thickness and mass loading of each layer were easily controlled by adjusting the mass of the materials for filtration. The electrodes and SE layers were then punched into discs with the desired size and stacked with high uniaxial pressure, as shown in Scheme 1**B**. To avoid edge shorting, the lateral size of the SE layer was a little larger than the cathode and anode layers. Stainless steel (SS) foil was selected as the bipolar plate because of its high electrical conductivity and good electrochemical stability in cathode and anode sides. Scheme 1**C** presents the bipolar stacked ASLBs and the detailed compositions in the mono cell. The advantage of bipolar stacked ASLBs is a high voltage, and the voltage value depends on the number of cells in stacking. For example, if one cell's voltage is 4.1 V, with double cells in series, the stack voltage is 8.2 V, as indicated in Scheme 1C. In our cells, high energy cathode and anode active materials were employed to boost the energy densities of the ASLBs. The cathode was based on a lithium silicate (Li_2SiO_x) coated S-NMC (Li_2SiO_x@S-NMC); the anode employed a Si composite; the thin SE membrane made of Li_6PS_5Cl was utilized. Both S-NMC and Si are proved

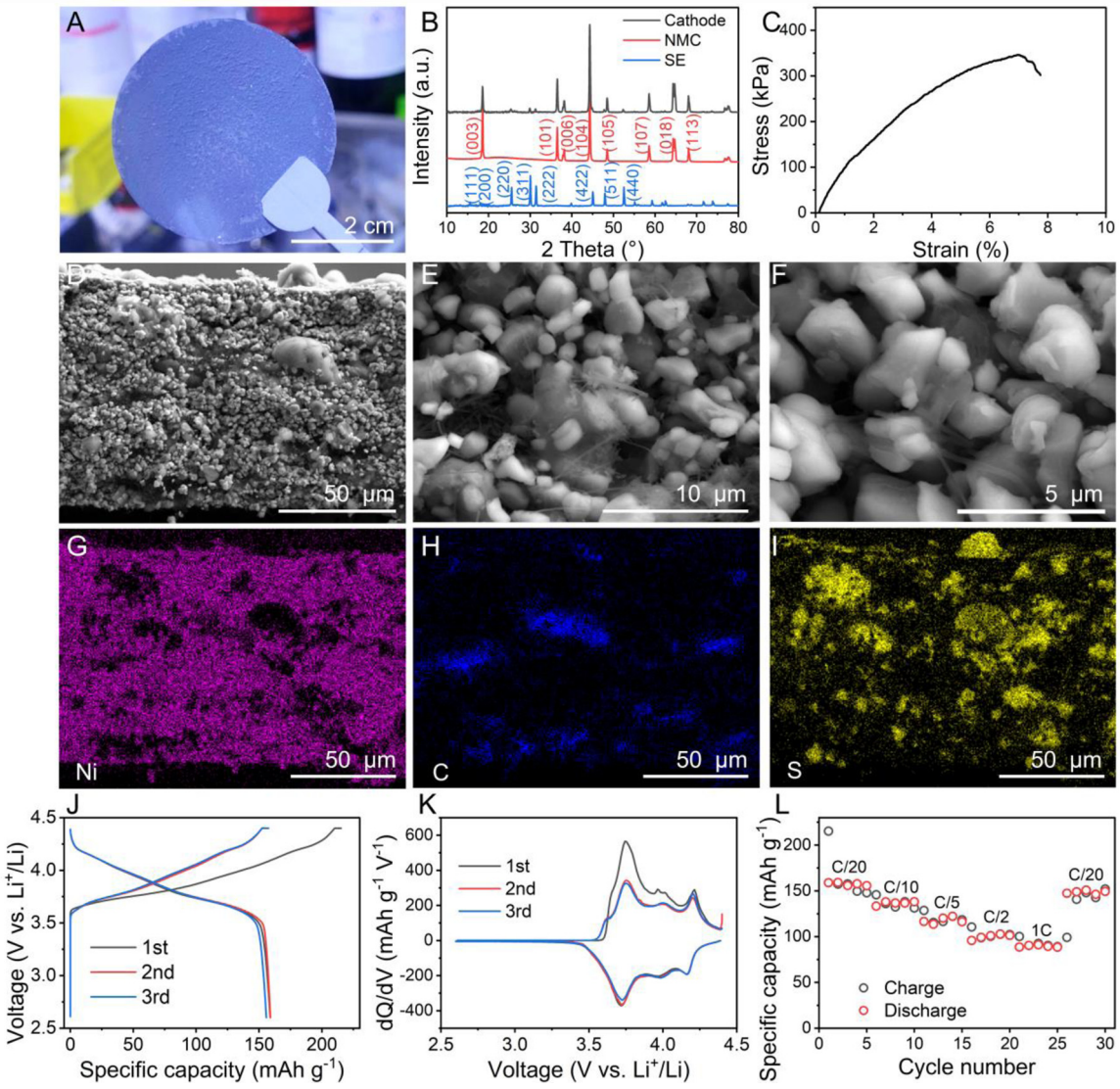

Fig. 1. Cathode layer characterization. (A) Photo of the cathode layer. (B) XRD patterns comparison among cathode layer and each component. (C) Tensile strength of the cathode layer. Cross-section SEM images of the cathode layer with magnitudes of (D) × 800, (E) × 5k, and (F) × 10k. EDX mapping of the cathode layer to show the distribution of (G) Ni, (H) C, and (I) S elements. (J) Charge/discharge profiles and (K) corresponding dQ/dV profiles of the cathode half cell at the first three cycles. (L) Rate performance of the cathode half cell.

with high energy [18–20]. The resulting cells were expected to deliver a high output voltage and cell-level high energy densities through bipolar stacking.

Fig. 1**A** displays the photo image of the as-prepared cathode layer. Highlight with good binding ability, ethyl cellulose with only 1.0 wt.% fraction enabled the cathode layer to be freestanding. The lateral size of the cathode layer is 44 mm, which can be further enlarged by using a larger filtration setup. Fig. 1**B** compares the X-ray diffraction (XRD) patterns of the cathode layer with the pristine Li_2SiO_x@S-NMC and Li_6PS_5Cl SE. All the peaks in the cathode are assigned to the S-NMC and Li_6PS_5Cl, and no newborn peaks are observed, suggesting the cathode fabricating process has no side reactions. The mechanical strength of the cathode layer was evaluated through the tensile test, as shown in Fig. 1**C**. A value of 347 kPa was obtained, which was sufficient in the following layers lamination and bipolar stacking.

Fig. 1**D–F** shows the SEM images of the cathode layer with a thickness of ~96 μm. The mass loading is ~25 mg cm^{-2}. The S-NMC owns an irregular morphology with an average particle size of ~3.8 μm, as shown in **Fig. S2**. The homogeneous and stable dispersion of S-NMC, Li_6PS_5Cl, and vapor grown carbon fibers (VGCF) in toluene results in a uniform and well-controllable layer thickness. Energy dispersive X-ray (EDX) mapping of Ni, C, and S elements also demonstrates the uniform dispersion of S-NMC, VGCF, and Li_6PS_5Cl in the cathode layer (Fig. 1**G–I**).

The electrochemical performance of the cathode layer was evaluated in a half cell with In-Li as the anode. Fig. 1**J** displays the charge and discharge profiles of the ASLB at C/20 at the first three cycles. There was a plateau starting from 3.63 V at the first charge process. In the following cycles, the plateaus were maintained with no obvious overpotential, demonstrating the Li_2SiO_x stabilized the interface between S-NMC and Li_6PS_5Cl [21]. High initial charge and discharge capacities of 215 and 159 mAh g^{-1} were achieved with a high initial coulombic efficiency (ICE) of 74.0%. No obvious capacity decay was observed in the following two cycles. The corresponding dQ/dV profiles were plotted to reveal the phase transition of S-NMC during cycling, as depicted in Fig. 1**K**. Three couples of anodic and cathodic peaks observed at 3.75 and 3.72, 4.00 and 3.98, 4.21 and 4.16 V are related to the phase transitions among monoclinic M, hexagonal H_1, H_2, and H_3 [22]. The profiles during discharge are almost overlapped, suggesting stable cycling. Then the rate performance of the cathode layer was investigated, as shown in

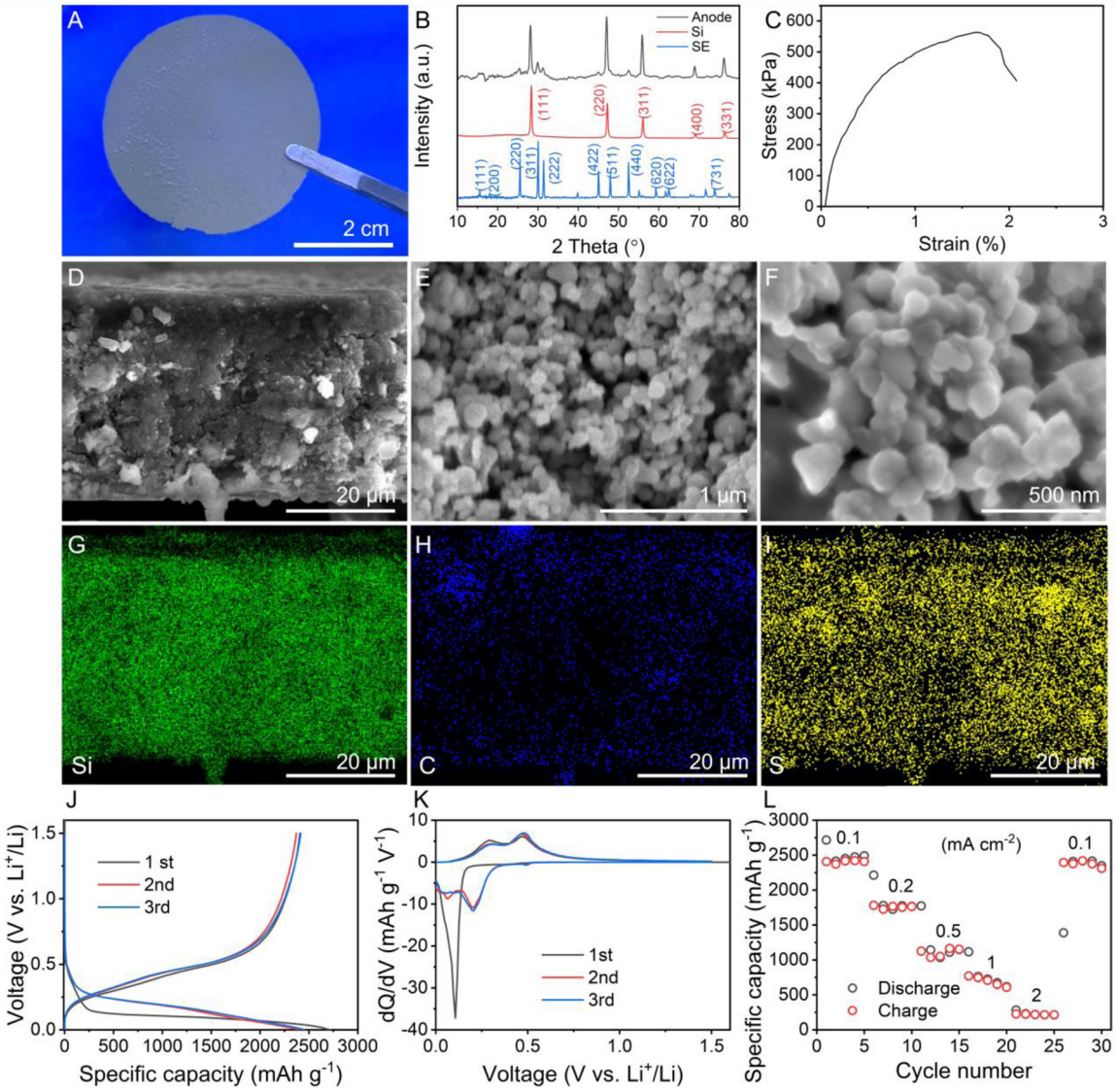

Fig. 2. Anode layer characterization. (A) Photo of the anode layer. (B) XRD patterns comparison among anode layer and each component. (C) Tensile strength of the anode layer. Cross-section SEM images of the anode layer with magnitudes of (D) × 2k, (E) × 50k, and (F) × 80k. EDX mapping of the anode layer to show the distribution of (G) Si, (H) C, and (I) S elements. (J) Charge/discharge profiles and (K) corresponding dQ/dV profiles of the anode half cell at the first three cycles. (L) Rate performance of the anode half cell.

Fig. 1**L**. The ASLB delivers average discharge capacities of 157, 136, 117, 100, and 89 mAh g^{-1} at the rate of C/20, C/10, C/5, C/2, and 1C, respectively. The capacity recovered to 148 mAh g^{-1} when recharged at C/20, evidencing an excellent rate performance and good cycling stability. **Fig. S3** shows the cross-section morphology of the cathode layer after the rate performance. The cathode maintained its integrity, and the mixture of NMC, SE, and VGCF was closely compacted. There was no delamination between the cathode and SE, suggesting excellent structure stability.

Fig. S4 displays the charge and discharge profiles of the ASLB using S-NMC cathode without adding ethyl cellulose. At the current rate of C/20, the ASLB delivered initial charge and discharge capacities of 217 and 167 mAh g^{-1} with a high ICE of 77.0 %. The performance is slightly higher than the one without adding a binder, demonstrating that adding a binder can reduce the capacity to some extent. Due to the ionic insulating, the binder blocks the electrode's ion conduction, resulting in reduced performance.

The anode layer was also investigated. Fig. 2**A** shows the photo image of the freestanding anode layer. The anode composes of nano Si, Li_6PS_5Cl, and carbon black in a weight ratio of 6:3:1. Due to the larger surface area of nano Si and carbon black than the cathode composite, the anode layer needs 4.0 wt% of ethyl cellulose to achieve good film formability and mechanical strength. The one with 2.0 wt.% ethyl cellulose was broken in the filtration process (**Fig. S5**). The mass loading of the anode layer is ~4 mg cm^{-2}. The XRD patterns of the anode layer shown in Fig. 2**B** all agree with the Si [23] and Li_6PS_5Cl [24], evidencing the filtration process has no side reactions. The anode layer delivered a high tensile strength of 562 kPa, as depicted in Fig. 2**C**, demonstrating its excellent processibility in the following full cell fabrication. Fig. 2**D–F** shows the cross section SEM images of the anode layer. The anode layer owns a uniform thickness of ~50 μm. The Si nanoparticles with an average particle size of 100 nm are aggregated into clusters, as shown in **Fig. S6**. After the ball milling, the Si nanoparticles are uniformly mixed with SE powder and carbon black. The EDX mapping of the anode layer, as show in Fig. 2**G–I**, evidences the uniform mixing of the three components.

The electrochemical performance of the anode layer was investigated in the half cell. Fig. 2**J** displays the charge and discharge profiles in the

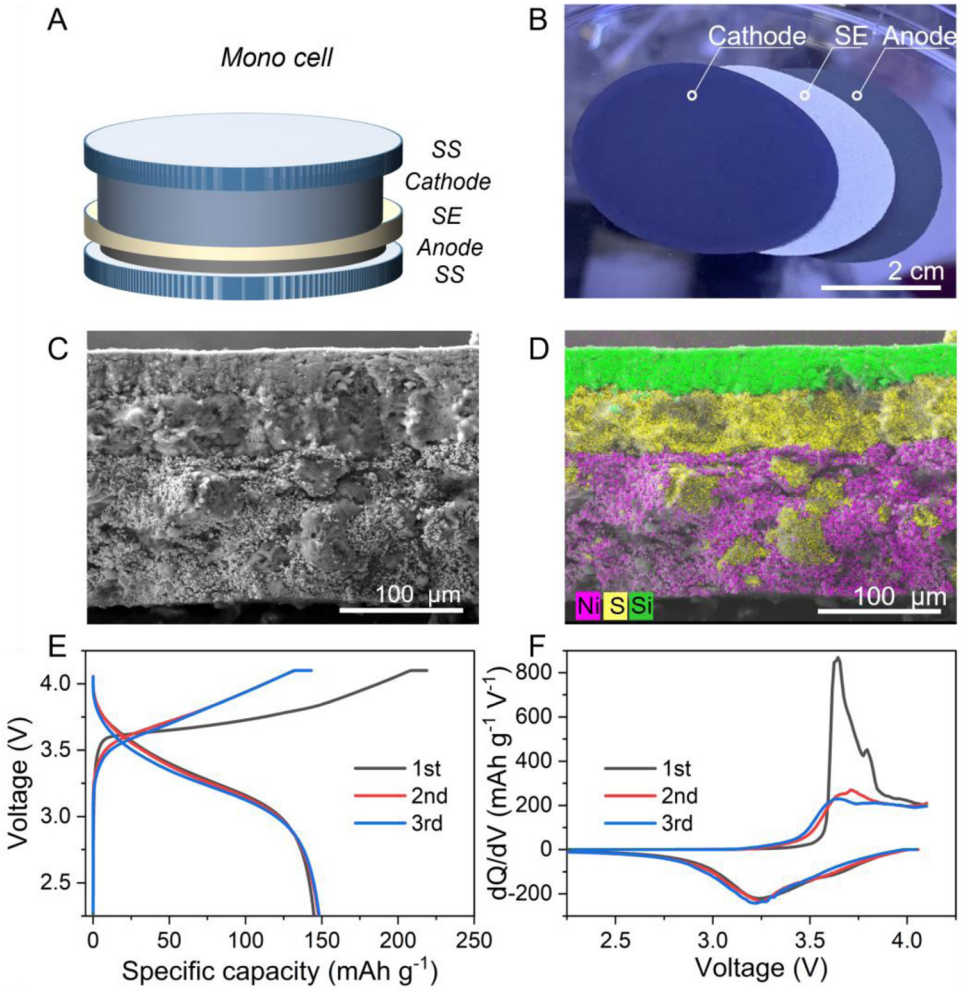

Fig. 3. Full cell performance of the mono cell. (A) Schematic illustration of the mono cell with lamination structure. (B) Photo of the freestanding cathode, SE, and anode layers used for full cell assembly. (C) SEM and (D) corresponding EDX mapping images to show the cross-section morphology of the mono cell. (E) Charge/discharge profiles and (F) dQ/dV curves of the mono cell in the initial three cycles at the current rate of 0.1 C.

first three cycles at the current density of 0.1 mA cm^{-2}. High initial charge and discharge capacities of 2700 and 2412 mAh g^{-1} are achieved with a high ICE of 89.3%. In the following two cycles, the capacity maintains stability. Fig. 2**K** shows the corresponding dQ/dV profiles. The obvious difference in the discharge profiles between the initial and following cycles is caused by the amorphization of Si after the first cycle. The two couples of reversible peaks located at 0.204/0.471 and 0.059/0.296 V present the transformations from different Li_xSi phases [25]. The rate performance of the anode layer is shown in Fig. 2**L**. At current densities of 0.1, 0.2, 0.5, 1, and 2 mA cm^{-2}, the ASLB delivers average capacities of 2404, 1757, 1104, 695, and 220 mAh g^{-1}. It presents that the addition of ethyl cellulose affects the rate performance of the anode layer a lot. When the cell was recharged at 0.1 mA cm^{-2}, the capacity recovered to 2375 mAh g^{-1}, demonstrating remarkable cycling stability. **Fig. S7** shows the cross-section morphology of the anode layer after cycling. The anode became denser after cycling in comparison to the pristine anode. It has been reported that the Si anode experienced an amorphization during cycling. In addition, the lithiated Si (Li_xSi) has more deformation than pure Si [18]. These explain the denser anode after cycling at a high stacking pressure. **Fig. S8** depicts the electrochemical performance of the composite anode without adding a binder. The ASLB delivered high discharge and charge capacities of 2841 and 2552 mAh g^{-1} with a high ICE of 89.8%. Similar to the cathode, the addition of the binder also causes a capacity reduction to the anode resulting from the hindered ion conduction by the binder.

Then the mono cell was assembled by facilely stacking the SS current collector, cathode layer, SE layer, and anode layer one by one, as illustrated in Fig. 3**A**. Here, a piece of freestanding SE membrane was utilized. The size of the SE was a little larger than the electrodes avoiding the direct contact of electrodes in cell assembling. Stainless steel foil with a low thickness of 10 μm was utilized as the current collector (or named monopolar plate) due to its superior electrochemical stability at both high and low potential. Under a uniaxial pressing, the stacked cathode, SE, and anode layers, as shown in Fig. 3**B**, are pressed together to fabricate the full cell. Fig. 3**C** displays the cross section SEM image of the full cell in which a layer-by-layer structure is observed. Specifically, the SE layers are much denser than the cathode and anode layers, avoiding mechanical failure. The EDX mapping in Fig. 3**D** presents the element distribution in three layers.

The mono cell was cycled at C/10 in the voltage range from 2.25 to 4.1 V. The n/p ratio was 1.45, calculated based on the half cell performance. Fig. 3**E** displays the charge and discharge profiles at the first three cycles. A high initial discharge capacity of 145 mAh g^{-1} was achieved with an ICE of 68.2%. In the following two cycles, the profiles almost overlapped with the initial cycle demonstrating good cycling stability. The corresponding dQ/dV profiles are depicted in Fig. 3**F**. Two pairs of anodic and cathodic peaks at 3.64 and 3.25, and 3.96 and 3.63 V are observed. The mono cell delivers high cell level gravimetric energy densities of 266 Wh kg^{-1} and 189 Wh kg^{-1} based on the mass with and without current collectors (see details in **Table S1**). The successfully assembled mono cell demonstrates the as-prepared cathode, SE, and anode layers own high processibility in cell fabrication.

The freestanding electrodes and SE layers enable the successful assembly of batteries series with bipolar design. As shown in Fig. 4**A**, in conventional stacked LIBs using liquid electrolyte, the unit cells are packed separately. In contrast, ASLBs can successfully address these lim-

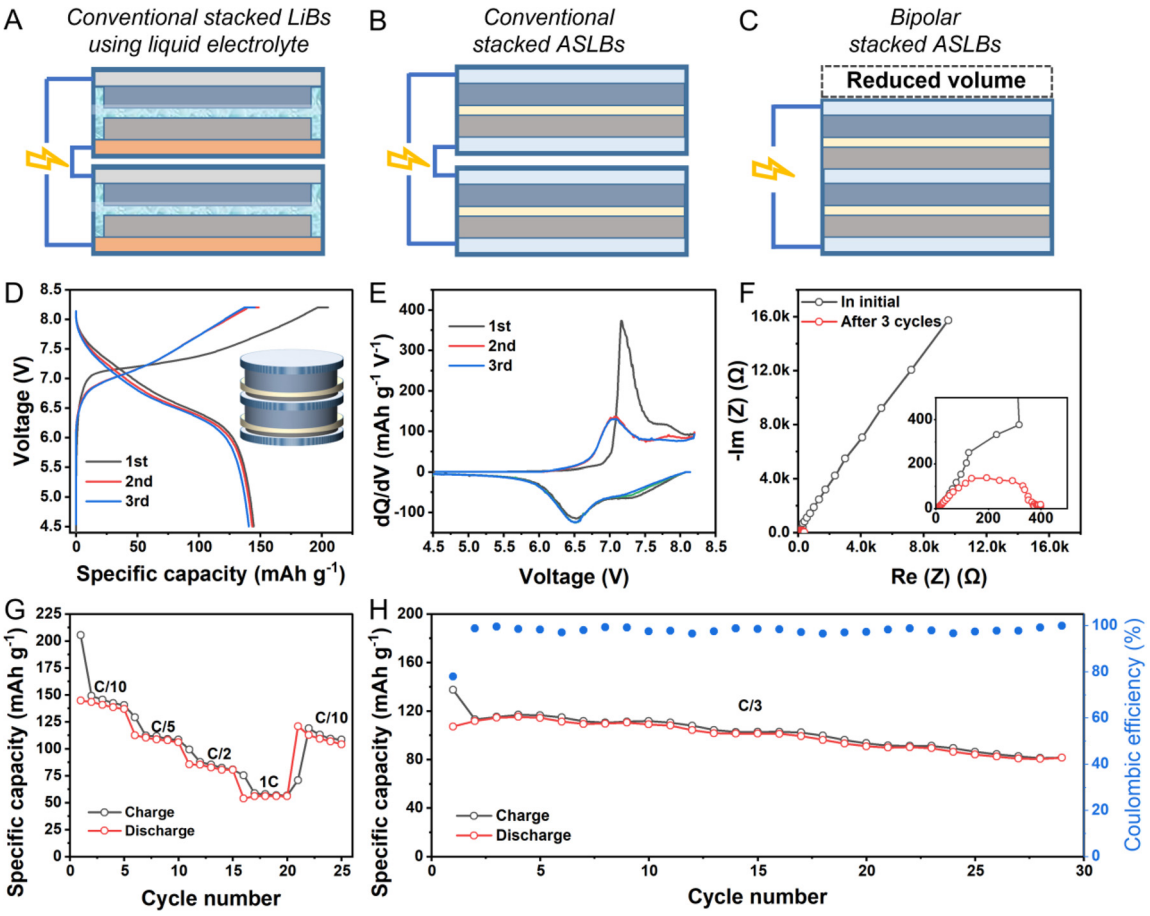

Fig. 4. Full cell performance of bipolar stacked ASLB. Schematic illustration of (A) conventional stacked LiBs using liquid electrolyte, (B) conventional stacked ASLBs, (C) Bipolar stacked ASLBs. (D) Charge/discharge profiles and corresponding (E) dQ/dV profiles at the first three cycles. Inset illustrates the architecture of the bipolar stacked ASLB. (F) Nyquist plots before and after the first three cycles. (G) Rate performances at the current rate of C/10, C/5, C/2, and 1C. (H) Cycling performance at the current rate of C/3.

itations. Fig. 4**B** and 4**C** compare the ASLBs in conventional stacking and bipolar stacking. Considering the SE is not flowable, the adjacent cells can directly contact each other, and all the cells can be packed together. Moreover, the adjacent cells can share one current collector, and the fraction of inactive material is greatly reduced. All these merits of solid cells with bipolar design contribute to a packing level high energy.

Fig. 4**D** displays the charge/discharge profiles in the initial three cycles at C/10 of the bilayer cell. The cells were successfully assembled and operated in a voltage range from 4.5 V to 8.2 V. An obvious plateau during charge was observed at around 7.2 V, agreeing with the doubled value in the mono cell, which demonstrates the good consistency between the two cells. High charge and discharge capacities of 205 and 145 mAh g^{-1} are achieved with an ICE of 70.7%. Fig. 4**E** presents the differential capacities with cell potential. Similarly, there are two pairs of peaks at 7.17 and 6.53 V, 7.83 and 7.33 V, which are double to the mono cell, demonstrating the consistency of these two cells. Fig. 4**F** shows Nyquist plots of the ASLB in initial and after three cycles. In the initial, there are only an incomplete semicircle and a Warburg tail. After three cycles, a depressed semicircle was observed with an impedance of ~400 Ω, agreeing with that of the mono cell. The rate performance was also evaluated. As shown in Fig. 4**G**, the cell delivers average specific capacities of 140, 110, 83, and 56 mAh g^{-1} at C/10, C/5, C/2, and 1C, respectively. The cell level gravimetric energy density of the ASLBs reaches 204 Wh kg^{-1}. The enhanced energy density compared with the mono cell is because of the less use of inactive materials. Another cell was assembled and measured at C/3, as depicted in Fig. 4**H**. A high initial capacity of 107 mAh g^{-1} was obtained. After 30 cycles, the capacity maintains at 81 mAh g^{-1}. The capacity fluctuation was caused by the temperature difference day and night in the lab.

The advance of the bipolar cell is evident when increasing the number of stacked cells. The cell level gravimetric energy densities of the ASLBs with bipolar stacking and conventional stacking are evaluated in Fig. 5. The calculation is based on the battery performance of the mono cell. Assume the adjacent mono cells in bipolar stacked ASLBs share one current collector and are packed together, while the mono cells in conventional stacked ASLBs own individual current collectors and packing (See details in **Table S2**). The energy density of the ASLBs with bipolar stacking rises from 189 Wh kg^{-1} to 217 Wh kg^{-1} as the connected cell number increases to 10. In contrast, the energy density of the ASLBs has no relationship with the number of connected mono cells. The energy density enhancement in bipolar stacked ASLBs can be much higher when considering the mass of packing materials and the connections. It demonstrates that the bipolar stacked ASLBs have great potential to deliver higher energy density than the conventional stacked ASLBs.

Great efforts are still needed in developing bipolar stacked ASLBs. **Table S3** compares the energy density and cycling life of reported sulfide SE-based ASLBs in serially bipolar stacking. By far, there are only two literature reported serially stacked bipolar studies based on sulfide ASLBs [15,26]. Our work delivers the highest energy density and longest cycling life. However, future efforts to further improve the performance of bipolar ASLBs are important. There are many challenges in devel-

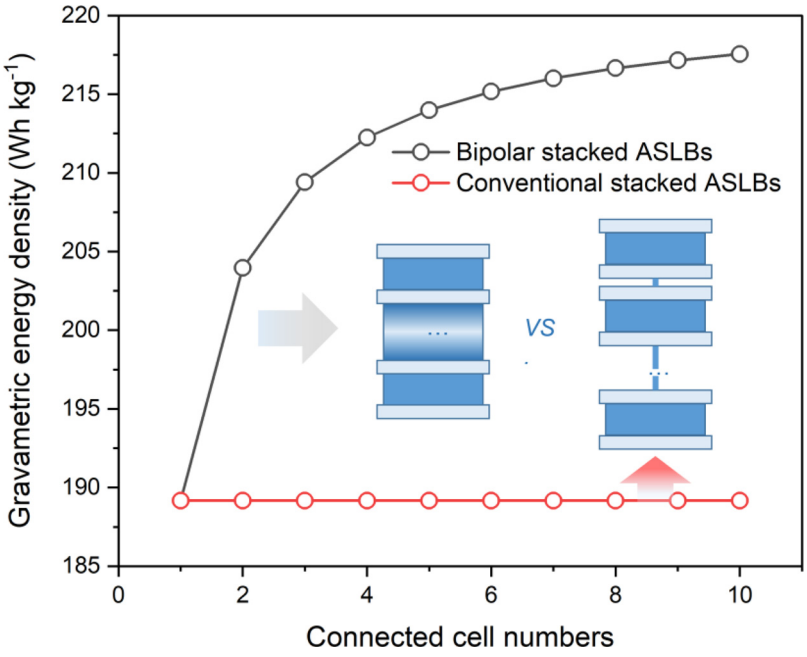

Fig. 5. Gravimetric energy density evaluation. The gravimetric energy density comparison between the bipolar stacked ASLBs and conventional stacked ASLBs.

oping high performance bipolar ASLBs. Firstly, the packed mono cells should have superior consistency. Because all the cells are cycled at the same current, the cut-off voltage is set based on the sum of the voltages. Any inconsistency among mono cells can lead to the overcharge of the mono cells resulting in quick performance fading. Secondly, the electrode volume expansion during cycling challenges the stability of the thin SE layer. Also, the anode and cathode shared one current collector. The volume change difference in cathode and anode brings mechanical failures. All these issues challenge the performance of the bipolar stacked ASLBs. More efforts are desired, like optimizing the binder, developing reliable electrodes and SE fabrication methods, increasing the mass fraction of active materials in electrodes, reducing the SE layer thickness, employing a thinner current collector, and so forth.

3. Conclusion

In summary, this work developed high energy density all-solid-state batteries based on sulfide electrolyte by employing high energy electrodes and unique bipolar stacking. In contrast to the conventional LiBs sealed separately and then packed together, the solid electrolyte (SE) enables ASLBs to be directly connected without extra packing materials. The bipolar stacking design minimizes inactive material in the batteries resulting in a significantly increased energy density. Moreover, since the batteries are connected in series, a high voltage output is obtained. Also, the shortened electron conduction paths between cells benefit lower resistance and increased power density.

Freestanding cathode, SE, and anode layers were fabricated through a facile vacuum filtration method based on an ethyl cellulose-toluene system. The cathode and anode layers showed considerable tensile strengths of 347 and 562 kPa, respectively, benefiting the fabrication of bipolar stacked ASLBs through facilely pressing the uniaxially stacked electrodes, SE, and current collector layers. A Li_2SiO_x coated single-crystal $LiNi_{0.8}Mn_{0.1}Co_{0.1}O_2$ and nano Si worked as the cathode and anode active material. Both cathode and anode delivered remarkable capacities. When coupled the cathode and anode layers in a mono cell, a cell-level high energy density of 189 Wh kg^{-1} (including current collectors) was obtained. In the bipolar-stacked double cell, the energy density was enhanced to 204 Wh kg^{-1}. This work sheds light on the significance of the bipolar design for ASLBs and accelerates the commercialization of ASLBs.

Declaration of Competing Interest

The authors declare no conflict of interest.

CRediT authorship contribution statement

Daxian Cao: Conceptualization, Methodology, Writing – review & editing, Investigation. **Xiao Sun:** Methodology, Investigation. **Ying Wang:** Methodology, Investigation. **Hongli Zhu:** Conceptualization, Writing – review & editing, Investigation, Supervision.

Acknowledgments

H. Z. acknowledges the financial support from National Science Foundation under Award Number CBET-ES-1924534. The authors acknowledge the Northeastern University Center for Renewable Energy Technology for the use of XRD am SEM facilities.

Supplementary materials

Supplementary material associated with this article can be found, in the online version, at doi:10.1016/j.ensm.2022.03.012.

References

[1] C. Wang, et al., All-solid-state lithium batteries enabled by sulfide electrolytes: from fundamental research to practical engineering design, Energy Environ. Sci. 14 (5) (2021) 2577–2619.
[2] Q. Zhang, et al., Sulfide-based solid-state electrolytes: synthesis, stability, and potential for all-solid-state batteries, Adv. Mater. 31 (44) (2019) 1901131.
[3] P.P. Paul, et al., Interfaces in all solid state Li-metal batteries: a review on instabilities, stabilization strategies, and scalability, Energy Storage Mater. 45 (2022) 969–1001.
[4] H. Zhang, et al., Electrolyte and anode-electrolyte interphase in solid-state lithium metal polymer batteries: a perspective, SusMat 1 (1) (2021) 24–37.
[5] Y. Gambe, Y. Sun, I. Honma, Development of bipolar all-solid-state lithium battery based on quasi-solid-state electrolyte containing tetraglyme-LiTFSA equimolar complex, Sci. Rep. 5 (1) (2015) 8869.
[6] J. Schnell, et al., All-solid-state lithium-ion and lithium metal batteries-paving the way to large-scale production, J. Power Sources 382 (2018) 160–175.
[7] M. Yamamoto, et al., Binder-free sheet-type all-solid-state batteries with enhanced rate capabilities and high energy densities, Sci. Rep. 8 (1) (2018) 1212.
[8] T. Famprikis, et al., Fundamentals of inorganic solid-state electrolytes for batteries, Nat. Mater. 18 (12) (2019) 1278–1291.

[9] Y. Chen, et al., Recent progress in all-solid-state lithium batteries: the emerging strategies for advanced electrolytes and their interfaces, Energy Storage Mater. 31 (2020) 401–433.
[10] Z. Wei, et al., Superior lithium ion conduction of polymer electrolyte with comb-like structure via solvent-free copolymerization for bipolar all-solid-state lithium battery, J. Mater. Chem. A 6 (27) (2018) 13438–13447.
[11] Z. Wei, et al., A large-size, bipolar-stacked and high-safety solid-state lithium battery with integrated electrolyte and cathode, J. Power Sources 394 (2018) 57–66.
[12] H.S. Shin, et al., Multilayered, bipolar, all-solid-state battery enabled by a perovskite-based biphasic solid electrolyte, ChemSusChem 11 (18) (2018) 3184–3190.
[13] K. Yoshima, Y. Harada, N. Takami, Thin hybrid electrolyte based on garnet-type lithium-ion conductor $Li_7La_3Zr_2O_{12}$ for 12 V-class bipolar batteries, J. Power Sources 302 (2016) 283–290.
[14] X. Chen, et al., Enhancing interfacial contact in all solid state batteries with a cathode-supported solid electrolyte membrane framework, Energy Environ. Sci. 12 (3) (2019) 938–944.
[15] J. Lee, et al., A nanophase-separated, quasi-solid-state polymeric single-ion conductor: polysulfide exclusion for lithium–sulfur batteries, ACS Energy Lett. 2 (5) (2017) 1232–1239.
[16] G. Homann, et al., High-voltage all-solid-state lithium battery with sulfide-based electrolyte: challenges for the construction of a bipolar multicell stack and how to overcome them, ACS Appl. Energy Mater. 3 (4) (2020) 3162–3168.
[17] D. Cao, et al., Amphipathic binder integrating ultrathin and highly ion-conductive sulfide membrane for cell-level high-energy-density all-solid-state batteries, Adv. Mater. 33 (52) (2022) 2105505.
[18] D.H.S. Tan, et al., Carbon-free high-loading silicon anodes enabled by sulfide solid electrolytes, Science 373 (6562) (2021) 1494–1499.
[19] C. Wang, et al., Interface-assisted *in-situ* growth of halide electrolytes eliminating interfacial challenges of all-inorganic solid-state batteries, Nano Energy 76 (2020) 105015.
[20] J. Wu, et al., All-solid-state lithium batteries with sulfide electrolytes and oxide cathodes, Electrochem. Energy Rev. 4 (1) (2021) 101–135.
[21] D. Cao, et al., Stable thiophosphate-based all-solid-state lithium batteries through conformally interfacial nanocoating, Nano Lett. 20 (3) (2020) 1483–1490.
[22] X. Dong, et al., Enhanced high-voltage cycling stability of Ni-rich cathode materials via the self-assembly of Mn-rich shells, J. Mater. Chem. A 7 (35) (2019) 20262–20273.
[23] B. Zhu, et al., Towards high energy density lithium battery anodes: silicon and lithium, Chem. Sci. 10 (30) (2019) 7132–7148.
[24] S. Wang, et al., High-conductivity argyrodite Li_6PS_5Cl solid electrolytes prepared via optimized sintering processes for all-solid-state lithium–sulfur batteries, ACS Appl. Mater. Interfaces 10 (49) (2018) 42279–42285.
[25] M.K. Datta, P.N. Kumta, *In situ* electrochemical synthesis of lithiated silicon–carbon based composites anode materials for lithium ion batteries, J. Power Sources 194 (2) (2009) 1043–1052.
[26] Y.J. Nam, et al., Bendable and thin sulfide solid electrolyte film: a new electrolyte opportunity for free-standing and stackable high-energy all-solid-state lithium-ion batteries, Nano Lett. 15 (5) (2015) 3317–3323.